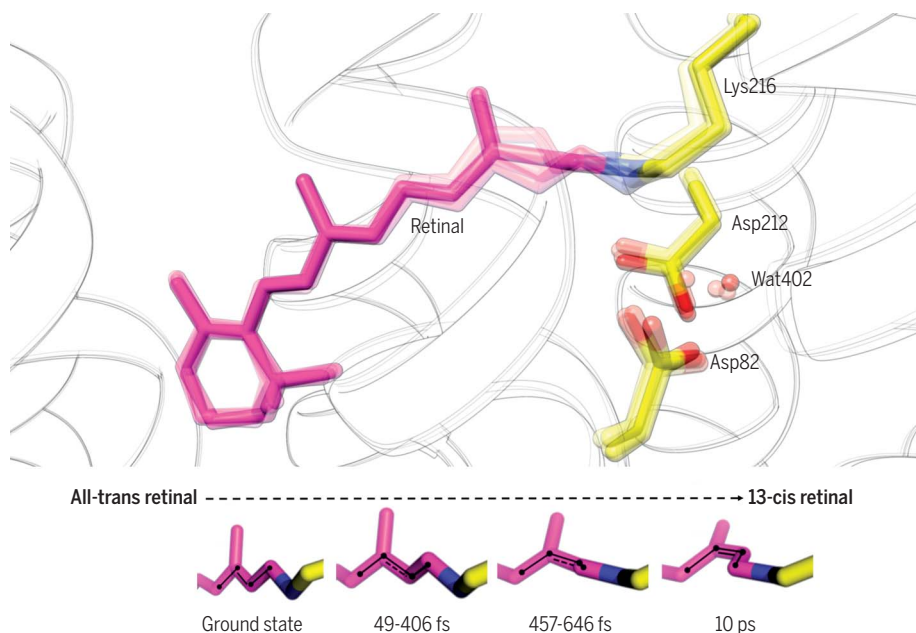# RESEARCH ARTICLE SUMMARY

## STRUCTURAL DYNAMICS

# Retinal isomerization in bacteriorhodopsin captured by a femtosecond x-ray laser

Przemyslaw Nogly, Tobias Weinert, Daniel James, Sergio Carbajo, Dmitry Ozerov, Antonia Furrer, Dardan Gashi, Veniamin Borin, Petr Skopintsev, Kathrin Jaeger, Karol Nass, Petra Båth, Robert Bosman, Jason Koglin, Matthew Seaberg, Thomas Lane, Demet Kekilli, Steffen Brünle, Tomoyuki Tanaka, Wenting Wu, Christopher Milne, Thomas White, Anton Barty, Uwe Weierstall, Valerie Panneels, Eriko Nango, So Iwata, Mark Hunter, Igor Schapiro, Gebhard Schertler, Richard Neutze, Jörg Standfuss*

**INTRODUCTION :** Retinal is a light-sensitive protein ligand that is used by all domains of life to process the information and energy content of light. Retinal-binding proteins are integral membrane proteins that drive vital biological processes, including light sensing for spatial orientation and circadian clock adjustment, as well as maintaining electrochemical gradients through ion transport. They also form the basis for optogenetic manipulation of neural cells. How the protein environment guides retinal isomerization on a subpicosecond time scale toward a single high-yield product is a fundamental outstanding question in photobiology.

**RATIONALE:** Light-induced isomerization of retinal is among the fastest reactions known in biology. It has been widely studied by spectroscopic techniques to probe the evolution of spectral intermediates over time. Using x-ray free-electron lasers (XFELs), it is now possible to observe ultrafast photochemical reactions

and their induced molecular motions within proteins on scales of femtoseconds to milliseconds with near-atomic structural resolution. In this work, we used XFEL radiation to study the structural dynamics of retinal isomerization in the light-driven proton-pump bacteriorhodopsin (bR). The principal mechanism of isomerization in this prototypical retinal-binding protein has direct relevance for all other members of this important family of membrane proteins, and it provides insight into how protein environments catalyze photochemical reactions in general.

**RESULTS:** We collected high-resolution x-ray diffraction data from bR microcrystals injected across the femtosecond x-ray pulses of the Linac Coherent Light Source after excitation of the retinal chromophore by an optical laser pulse. X-ray diffraction images were sorted into temporal subgroups with a precision of about 200 fs. A series of 18 overlapping difference Fourier electron density maps reveal structural changes over the first picosecond of retinal photoexcitation. Complementary data for time delays of 10 ps and 8.33 ms allow us to resolve the later stages of the reaction. In combination with refined crystallographic structures at pump-probe delays corresponding to where the spectroscopically characterized I, J, K, and M intermediates form in solution, our time-resolved structural data reveal the trajectory of retinal isomerization and provide atomic details at key points along the reaction.

The aspartic acid residues of the retinal counterion and functional water molecules in close proximity to the retinal Schiff base respond collectively to the formation and decay of the excited state. This collective motion sets the stage for retinal isomerization, which proceeds via a twisted retinal configuration. Quantum mechanics/molecular mechanics simulations provide theoretical support for this structural evolution.

**ON OUR WEBSITE**

Read the full article at http://dx.doi.org/10.1126/science.aat0094

**CONCLUSION:** Our observations reveal how, concomitant with the formation of the earliest excited state, the retinal-binding pocket opens up in close proximity to the isomerizing bond. We propose that ultrafast charge transfer along retinal is a driving force for collective motions that contribute to the stereoselectivity and efficiency of retinal isomerization within a protein scaffold. Vibrational quake-like motions extending from retinal to the protein may also be a mechanism through which excess energy is released in a nonradiative fashion. ∎



**Time-resolved serial crystallography resolves ultrafast atomic motions of retinal and the surrounding protein following photoexcitation.** Retinal evolves from an all-trans conformation in the ground state toward a twisted 13-cis retinal over the course of a few hundred femtoseconds. The complex counterion, formed by two aspartic acid residues (Asp) and a water molecule (Wat), responds to changes in the electronic structure of the chromophore on the same time scale as the formation of the excited state.

# RESEARCH ARTICLE

## STRUCTURAL DYNAMICS

# Retinal isomerization in bacteriorhodopsin captured by a femtosecond x-ray laser

Przemyslaw Nogly[1], Tobias Weinert[1,2], Daniel James[1], Sergio Carbajo[3], Dmitry Ozerov[4], Antonia Furrer[1], Dardan Gashi[5], Veniamin Borin[6], Petr Skopintsev[1], Kathrin Jaeger[1], Karol Nass[5,2], Petra Båth[7], Robert Bosman[7], Jason Koglin[3], Matthew Seaberg[3], Thomas Lane[3], Demet Kekilli[1], Steffen Brünle[1], Tomoyuki Tanaka[8,9], Wenting Wu[1], Christopher Milne[5], Thomas White[10], Anton Barty[10], Uwe Weierstall[11], Valerie Panneels[1], Eriko Nango[8,9], So Iwata[8,9], Mark Hunter[3], Igor Schapiro[6], Gebhard Schertler[1,12], Richard Neutze[7], Jörg Standfuss[1]*

Ultrafast isomerization of retinal is the primary step in photoresponsive biological functions including vision in humans and ion transport across bacterial membranes. We used an x-ray laser to study the subpicosecond structural dynamics of retinal isomerization in the light-driven proton pump bacteriorhodopsin. A series of structural snapshots with near-atomic spatial resolution and temporal resolution in the femtosecond regime show how the excited all-trans retinal samples conformational states within the protein binding pocket before passing through a twisted geometry and emerging in the 13-cis conformation. Our findings suggest ultrafast collective motions of aspartic acid residues and functional water molecules in the proximity of the retinal Schiff base as a key facet of this stereoselective and efficient photochemical reaction.

Organisms harvest light for its energy and information content. Seven-transmembrane-helix retinal proteins use the absorption of photons to achieve both of these purposes across all domains of life. Family members include visual rhodopsins (light receptors triggering vision) in animals, as well as bacteriorhodopsin and proteorhodopsins (proton pumps), halorhodopsins (anion pumps), channelrhodopsins (gated ion channels), and sensory rhodopsin (phototaxis receptors) in archaea and bacteria. Retinal-binding ion pumps and channels have found exciting applications in the optogenetic manipulation of neural cells (*1*).

Activation of seven-transmembrane-helix retinal proteins is initiated by the photochemical trans-to-cis (or cis-to-trans for visual rhodopsins) isomerization of the conjugated double bond system of the retinal chromophore. Photo-isomerization is one of the fastest reactions in biology, being completed within a few picoseconds after photon absorption. Retinal isomerization occurs stereoselectively at a specific double bond within the binding pocket of the protein host and with a quantum yield of up to 67% (*2*, *3*). In contrast, illumination of all-trans retinal in solution leads to formation of a mixture of different stereoisomers—13-cis, 11-cis, and 9-cis—with a quantum yield of only a few percent for each subproduct (*4*). How the protein scaffold rapidly guides retinal isomerization toward a single high-yield product is an outstanding and fundamental question in photobiology.

Bacteriorhodopsin (bR) is an archetypical proton pump that has long served as a system for understanding how the energy of a captured photon may be used to achieve unidirectional proton transport against a transmembrane proton concentration gradient. Chemical insights into retinal isomerization have emerged from ultrafast spectroscopy, which identified the I, J, and K intermediates rising and decaying in the ultrafast time regime (Fig. 1) (*5*–*8*). Hybrid quantum mechanics/molecular mechanics (QM/MM) simulations have provided further insight into the initial steps of retinal isomerization, including predictions of energy and charge redistributions (*9*). Despite

these advances, theoretical and spectroscopic studies require complementary structural information to build a complete picture of the highly efficient photo-isomerization of retinal within proteins. Researchers have described reaction-cycle intermediates from x-ray structures after illuminating crystals with visible light at low temperatures or changing their pH (*10*). Such intermediate-trapping studies, however, have yielded conflicting results for the earliest available structural intermediate, K (*11*–*13*). Importantly, they cannot address the first events upon photo-isomerization because the low thermal energy barriers are not rate-limiting on the ultrafast time scale.

With the advent of x-ray free-electron lasers (XFELs), time-resolved serial femtosecond crystallography (TR-SFX) has emerged as a powerful method to study ultrafast structural changes in proteins (*14*). TR-SFX was validated against time-resolved Laue diffraction recorded at a synchrotron radiation source, using photoactive yellow protein (PYP) as a model system (*15*). The method has further provided insight into ultrafast structural changes during the photodissociation of carbon monoxide from the active site of myoglobin (*16*), isomerization of *p*-coumaric acid in PYP (*17*), and isomerization of hydroxybenzylidene imidazolinone in rsEGFP2 (reversibly photoswitchable green fluorescent protein 2) (*18*). TR-SFX has also tracked the evolution of protein and water molecule rearrangements in bR from nanoseconds to milliseconds, from which a coherent picture of proton pumping has emerged (*19*). We used this powerful new methodology to characterize the photo-isomerization of retinal and the immediate adaptations of its protein binding pocket.

X-ray diffraction data were collected to 1.50-Å resolution (table S1) from a continuous stream of light-adapted bR microcrystals grown in a lipidic cubic phase (LCP) (*20*, *21*) at the coherent x-ray imaging (CXI) beamline (*22*) of the Linac Coherent Light Source (LCLS) (*23*). About 1 million indexable diffraction patterns were collected in a pump-probe scheme using a sequence of four x-ray probe pulses between every optical pump laser pulse (fig. S1) (*24*). The x-ray diffraction images immediately following the optical laser pulse at four nominal delays were sorted into subgroups based on the LCLS timing tool signal (*25*) with a temporal resolution estimated to be on the order of 200 fs (*16*, *17*) (fig. S2). Sequential windows of data within the first picosecond [overlapping pump-probe delay ($\Delta t$) ranges with ~30,000 sorted diffraction patterns], together with data collected at $\Delta t = 10$ ps and $\Delta t = 8.33$ ms, yielded 20 snapshots of bR activation.

### Trajectory of retinal isomerization

A long-distance overview of electron density changes ($F_{obs}^{light} - F_{obs}^{dark}$) in bR during the course of the first 10 ps is shown in movie S1. Changes are already visible for the earliest time point and are initially clustered at the retinal and its binding pocket. A close-up view of the retinal chromophore (Fig. 2 and movie S2) reveals negative density features that are visible above

**Fig. 1. Early events in bacteriorhodopsin (bR) activation.** (**A**) Structural changes in the seven-transmembrane-helix proton-pump bR are initiated by the trans-to-cis isomerization of the covalently bound retinal chromophore. The arrows indicate the direction of $H^+$ transport from the cytoplasmic side (IC) to the extracellular side (EC) of the membrane. A hydrogen-bonding network including the complex counterion network and several water molecules is critical for maintaining the high affinity of the Schiff base (SB) link for protons. (**B**) Serial femtosecond crystallography allows us to resolve the retinal molecule and its binding pocket with near-atomic resolution ($2F_{obs} - F_{calc}$ electron density of the light-adapted resting state at 1.5-Å resolution shown in gray at $2\sigma$) at ambient temperature and in the membrane-like environment of lipidic cubic phases. The atoms C13 and C14 are labeled to indicate the bond undergoing isomerization. (**C**) The retinal chromophore (sticks with van der Waals radii shown as translucent halos) is tightly encased within the binding pocket of the bR dark state (yellow). (**D**) Retinal isomerization is an ultrafast event progressing within picoseconds from the



bR dark state through the I and J intermediates to the K intermediate. I forms within about 200 fs after excitation and is characterized by a rapid rise in the retinal dipole moment (5) and twisting of the polyene backbone (6). After about 500 fs, the J intermediate evolves, which initiates the isomerization reaction (7) and turns into the K state with isomerized 13-cis retinal after about 3 ps (8). The ultrafast dynamic interplay between retinal and its binding pocket increases quantum efficiency and guides stereoselectivity of retinal isomerization.
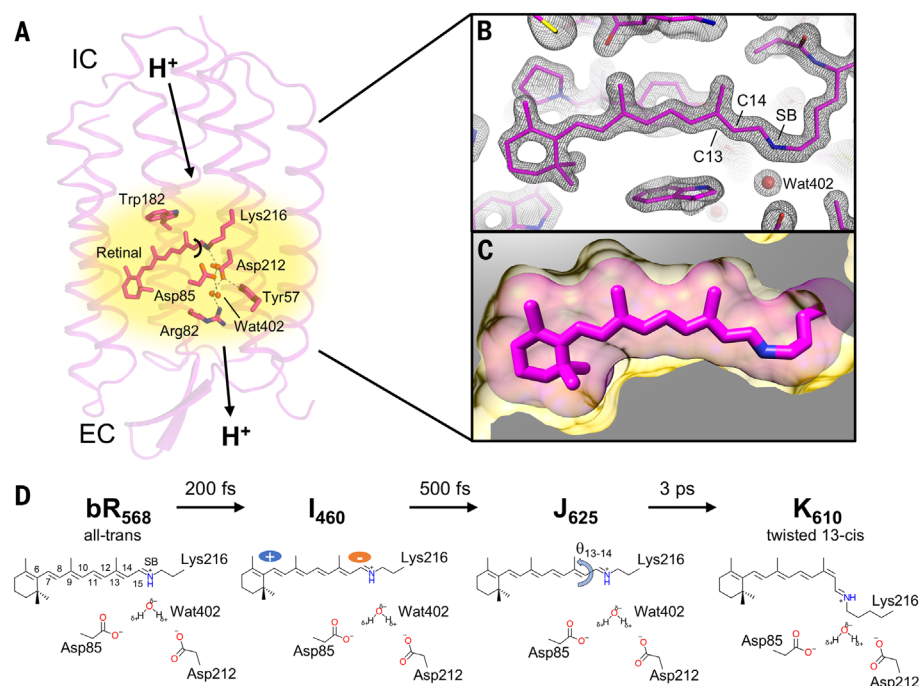
**Fig. 2. Femtosecond structural dynamics along the retinal chromophore.** (**A**) The potential energy diagram (energy, $y$ axis; reaction coordinates, $x$ axis) indicates how absorption of a photon promotes all-trans retinal to the Franck-Condon point (FC). The excitation energy is kinetically dissipated after passage through the conical intersection (CI). Trans-cis isomerization occurs along local energy minima correlating with the I, J, and K spectroscopic intermediates. According to the commonly accepted model, the transition of the excited-state intermediate I to the first ground-state product J occurs within about 0.5 ps and coincides with the onset of retinal isomerization (7, 27, 59). (**B** to **E**) The progression of difference Fourier electron density ($F_{obs}^{light} - F_{obs}^{dark}$, contoured at $4\sigma$; gold, negative; blue, positive) displayed along a dark-state model allows us to follow the trans-cis transition and see how the double bond system is sampled immediately after photoactivation, before selective isomerization around the C13=C14 bond occurs. The process results in an energetically elevated 13-cis isomer that is still twisted by the protein binding pocket 10 ps after activation. All temporal snapshots of this trajectory are available as movie S2.
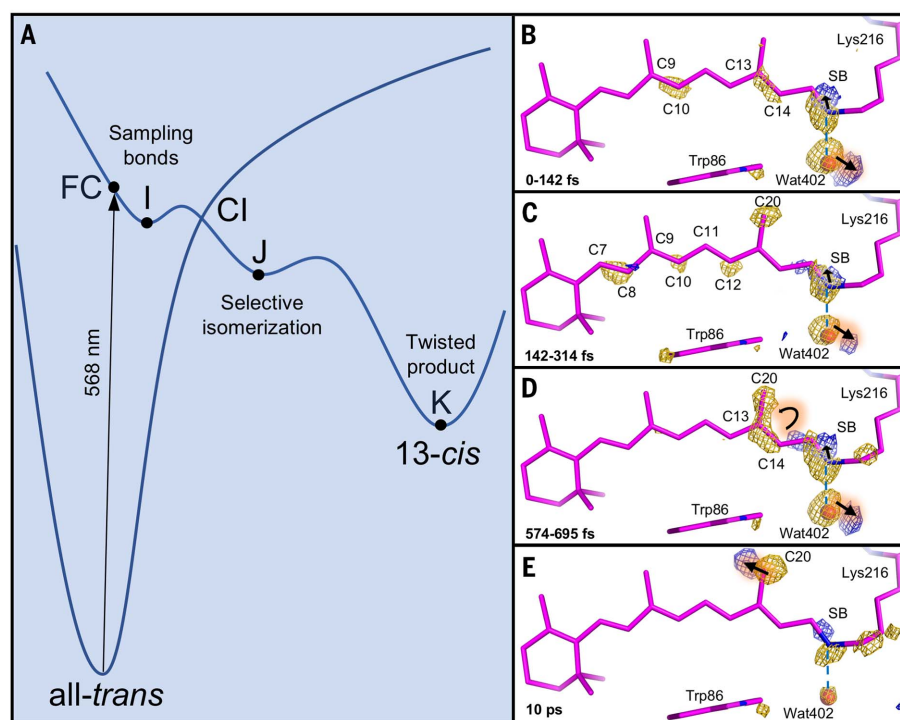


$4\sigma$ ($\sigma$ is the root mean square deviation of electron density) on the carbon atoms of the retinal polyene backbone (associated with C8, C10, C12, and C14) and corresponding weaker positive features (2.7$\sigma$ to 4.4$\sigma$; table S3) for $\Delta t \leq 500$ fs, but which decay for later time delays. Theoretical analyses have argued that photon absorption induces a partial charge relocation in retinal from the Schiff base (SB) toward the β-ionone ring in the excited state and before the trans-to-cis isomerization (9). Measurements of transient changes in the excitonic coupling between the retinal dipole moment and nearby tryptophan residues imply that this charge redistribution occurs within 200 fs after photon absorption (5).

Simultaneously, nuclear rearrangements lead to an extension of double bonds and contraction of the single bonds (so-called inversion of the bond length alternation), which allows the planar geometry of retinal to distort in the excited state (26). Such distortion is consistent with the negative and (weaker) positive features of the difference Fourier electron density map ($F_{obs}^{light}$ –
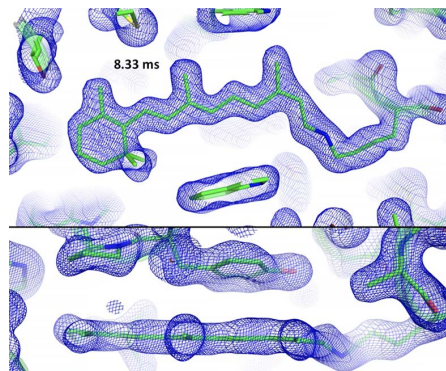


**Movie 1. Retinal isomerization in refined structures with extrapolated electron density ($2F_{ext} − F_{calc}$, contoured at 1.2σ).**
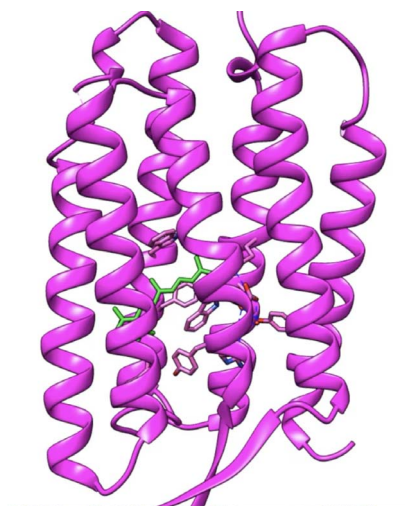


**Movie 2. Dynamic view of retinal isomerization and response of the counterion network.** The movie shows the transitions between four structural intermediates: ground state, $\Delta t$ = 49 to 406 fs, $\Delta t$ = 457 to 646 fs, and $\Delta t$ = 10 ps. The morphs between the refined structures were generated with Chimera (60) and reveal a fast motion proceeding through the entire structure, followed by a slower rearrangement. A zoom-in to the region of the counterion network highlights the hydrogen-bond breakage between the SB and Wat[402] (W 402). The detailed view of the retinal isomerization visualizes the structural rearrangements as the isomerization proceeds. Time scales in the movie do not correlate to real time scales, and the structures are linear morphs of atom motions. The 457 to 646 fs → 10 ps transition is shown more slowly than the other two transitions to highlight the longer time scale of the transition.

$F_{obs}^{dark}$) observed around the C7 to C14 atoms of the retinal on this time scale (Fig. 2).

The retinal initially samples possible isomerization geometries for $\Delta t$ ≤ 500 fs, but the possible evolution is heavily constrained by the rigidity of the binding pocket. After this sampling of double bond geometries in the initial excited state, electron density changes focus around the C13=C14 double bond, suggesting a coordinated evolution throughout the trans-cis isomerization. The progress of retinal isomerization can be followed in extrapolated electron density maps (fig. S3 and Movie 1). Changes over time are best visualized by overlaying the difference Fourier electron density map with the resting and refined structures for the time ranges $\Delta t$ = 49 to 406 fs, 457 to 646 fs, 10 ps, and 8.33 ms (table S2) with Fig. 3. These time windows correlate approximately with accumulation of the spectroscopically distinct I, J, K, and M intermediates identified in solution (5–8, 27, 28). In the earliest temporal windows, paired difference density features indicate that the retinal SB nitrogen is already displaced toward helix G, which is quantified by structural refinement as a 0.5-Å sideways motion of the SB but with the retinal geometry otherwise remaining similar to the all-trans conformation. For $\Delta t$ =

457 to 646 fs, a stronger continuous negative difference is apparent along the C20–C13=C14 bonds, and two positive difference density peaks flank a negative feature on the SB nitrogen. This time point is modeled as a twisted retinal configuration with the C12–C13=C14–C15 torsion angle ~90° and the C15=Nζ bond lying in the plane of the membrane. Overall changes between the dark and $\Delta t$ = 457 to 646 fs time delay twist the torsion angles of the C13=C14 and the neighboring C11=C12 and C15=Nζ bonds in opposite directions, indicating that the reaction proceeds according to the aborted bicycle-pedal model of retinal isomerization (9, 29, 30).

By $\Delta t$ = 10 ps, only one positive feature remains in the difference Fourier electron density map that is complementary to the negative peak on the SB nitrogen atom, and paired positive and negative density features are associated with the retinal C20 methyl group. Structural refinement indicates that these changes represent the retinal having reached its twisted 13-cis configuration and the C20 methyl being twisted toward helix G. This sequence of events is entirely consistent with QM/MM simulations of the retinal excited state when the key water molecule (Wat[402]), Lys[216], and the counterion network are included
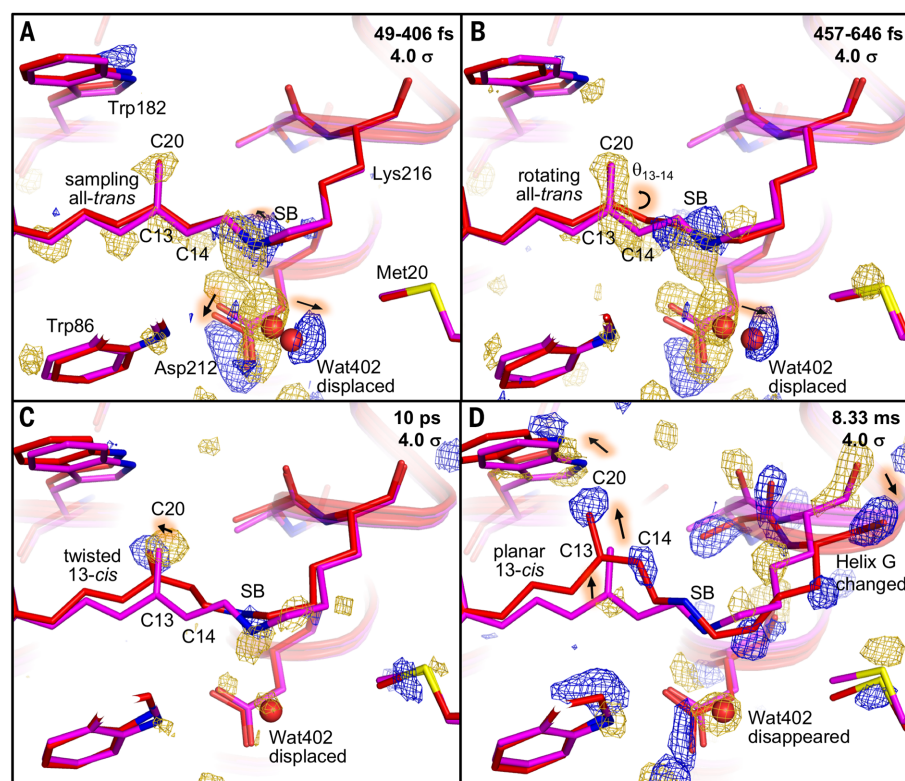


**Fig. 3. Structural intermediates at pump-probe delays ($\Delta t$) corresponding to times when key spectral intermediates of the bR photocycle occur.** (A) $\Delta t$ = 49 to 406 fs, I intermediate. (B) $\Delta t$ = 457 to 646 fs, J intermediate. (C) $\Delta t$ = 10 ps, K intermediate. (D) $\Delta t$ = 8.33 ms, M intermediate. The structure of the bR dark state is shown in magenta and overlaid with the bR reaction intermediates in red. The difference Fourier electron density map ($F_{obs}^{light} − F_{obs}^{dark}$, contoured at 4σ; gold, negative; blue, positive) and arrows indicate the structural rearrangements around the isomerizing C13=C14 bond and the retinal counterion. The corresponding extrapolated electron density maps ($2F_{ext} − F_{calc}$) are available as fig. S3 and Movie 1.
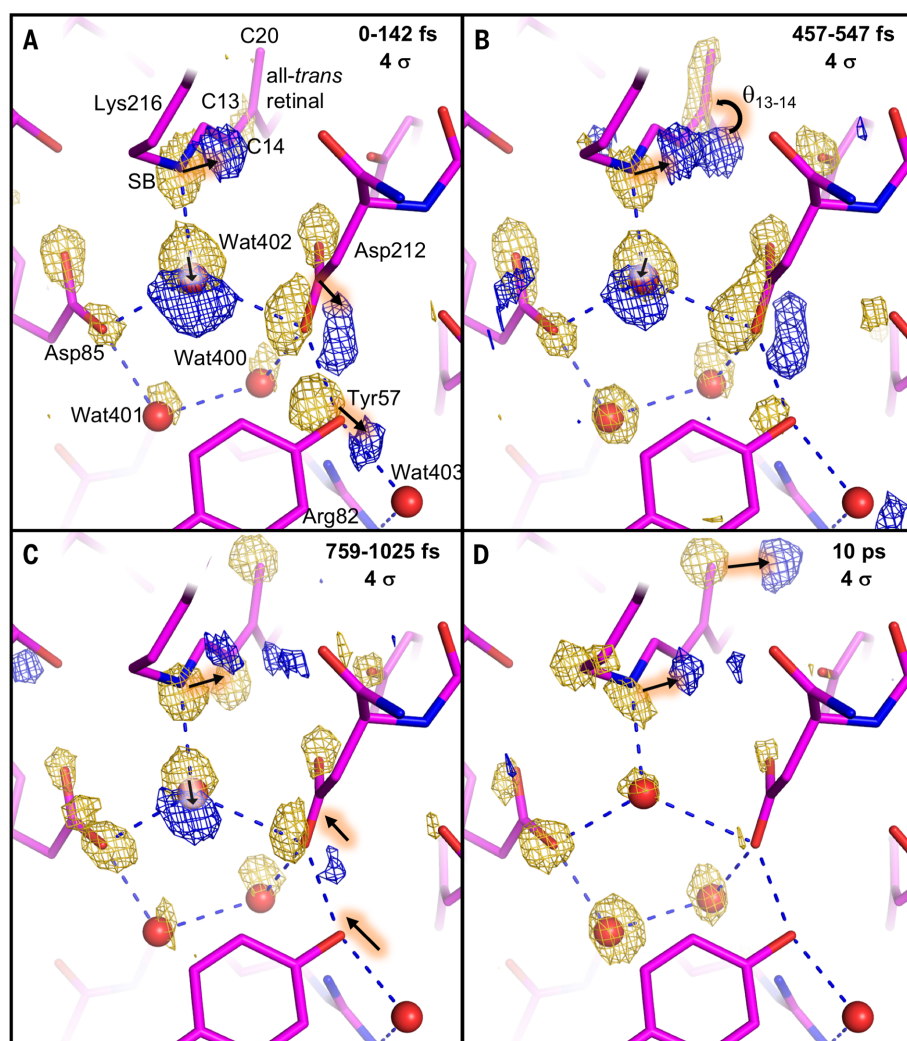
**Fig. 4. Close-up view of the protonated SB and associated counterion network. (A to D)** Progression of the difference Fourier electron density map ($F_{obs}^{light} - F_{obs}^{dark}$, contoured at 4σ; gold, negative; blue, positive) shows the coherent motions of the hydrogen-bonding network connecting the SB with Asp[85], Asp[212], and Tyr[57] via water molecules Wat[402], Wat[401], and Wat[400]. Arrows indicate correlated motions in retinal and the hydrogen-bonding network. The sticks represent the dark-state model of bR. All temporal snapshots are available as movie S3.

within the quantum chemical description [fig. S4 and (*9*)], providing theoretical support for the structural evolution that we observed. Lastly, the difference Fourier electron density map recorded for $\Delta t$ = 8.33 ms displays all major features previously observed for $\Delta t$ = 1.725 ms (*19*), including the planar 13-cis retinal characteristic of later reaction intermediates of the bR photocycle.

### Ultrafast response of the counterion cluster

A key feature in the resting bR state is a hydrogen bond (H-bond) interaction of the SB with Wat[402], which participates in the H-bonding network with the counterions Asp[85] and Asp[212] and stabilizes the positive charge on the SB nitrogen (*31*). Mutation of either Asp[85] or Asp[212] to noncharged residues greatly reduces the rate of retinal

isomerization (*32*), and both have been implicated in guiding stereoselectivity of the reaction (*33*).

Wat[402] and the SB respond to the photon absorption of retinal even before the isomerization appears to begin, moving up to 0.6 Å further away from each other (to a distance of 3.25 Å) after light absorption ($\Delta t$ = 49 to 406 fs). This separation increases to 4.05 Å once the retinal is isomerized ($\Delta t$ = 10 ps). This movement is visualized as very strong, paired positive and negative features in the difference Fourier electron density map (from 6σ to 11σ; Fig. 4) associated with Wat[402], Asp[212], and Tyr[57], which together reveal an ultrafast collective motion of a group of polar residues connected through H-bond interactions (Movie 2). The driving force for this motion is the ultrafast redistribution of the positive charge away from the SB and toward the β-ionone ring.

Quantum chemical calculation of the difference between the ground- and excited-state electron density (fig. S4) shows the localization of changes along the retinal polyene chain. The sudden polarization instantaneously pushes the water molecule away from the SB (up to a distance of 3.65 Å at $\Delta t$ = 457 to 646 fs) and breaks the SB–Wat[402] H-bond (which would otherwise oppose the SB reorientation during isomerization). Loss of the H-bond lowers the energy barrier for a specific isomerization pathway (*34*), allowing the retinal to isomerize about the C13=C14 bond. These collective motions are later damped, with the retinal being fully isomerized at $\Delta t$ = 10 ps, while Wat[402] loses its interaction with the SB, consistent with a changing H-bonding pattern in this region predicted by low-temperature Fourier transform infrared (*35*) and Raman spectroscopy (*36*). The rigidity of the large hydrophobic region of the retinal-binding pocket, which prevents unwanted C7=C8, C9=C10, or C11=12 cis products, is in stark contrast with the specific ultrafast motions associated with Wat[402] and the counterion cluster. These findings implicate ultrafast collective motions as an essential ingredient for efficient isomerization within the protein scaffold.

### Protein quake

The collective motions from the counterion region extend up to 12 Å away from the SB nitrogen within 600 fs (fig. S5) yet become dispersed on longer time scales. This dampening is evidenced by weaker paired difference densities associated with Tyr[57] at $\Delta t$ = 759 to 1025 fs, as well as the motions of Thr[47] and Asp[212], which are no longer visible at $\Delta t$ = 10 ps. Changes are further apparent when comparing the refined structural intermediates at $\Delta t$ = 49 to 406 fs, 457 to 646 fs, and 10 ps (Movie 2). As such, these motions propagate away from the active site at 2 nm/ps, which is noticeably faster than the speed of sound in water (~1.5 nm/ps). These observations are consistent with the propagation of motions in the bacterial photoreaction center (*37*) and myoglobin (*16*, *38*, *39*) and the theory of protein quakes that suggests how excess energy in proteins can be dissipated in earthquake-like motions of collective structural deformations (*40*). In the case of photoactive proteins such as bR, these motions may be the mechanism through which excess energy from decay of the excited state is released in a nonradiative fashion.

Our ultrafast TR-SFX data recorded using an XFEL captures a fundamental photochemical reaction and one of the fastest processes in biology. In particular, our measurements uncover the initial structural rearrangements in the excited state that guide the selective isomerization process. Photo-excited retinal initially samples multiple isomerization pathways within its binding pocket, but the ultimate fate of the reaction is steered by the near-instantaneous charge redistribution along the retinal and the resulting collective motions of the SB counterion complex. Breaking of the SB–Wat[402] H-bond enables the trans-to-cis isomerization about the C13=C14 double bond. Similar ultrafast collective motions may guide

the stereochemistry and enhance the quantum efficiency of retinal isomerization in such diverse processes as phototrophy in the seas, neuron stimulation in optogenetics, and the initiation of visual signals within the photoreceptors of our eyes.

## Materials and methods
### Purification and crystallization of bR

Bacteriorhodopsin was purified from purple membranes of *Halobacterium salinarum*. The purification and crystallization was performed as described previously (*24, 41*) with a few modifications. The purple membranes were solubilized overnight in the presence of 1.7% β-octylglucoside (Anatrace) and 50 mM sodium phosphate buffer pH 6.9 (GERBU). After solubilization the pH was adjusted to 5.5 with 0.1 M HCl and the insoluble fraction was removed by 1-hour centrifugation at 150 000 × *g*. The size exclusion purification step was omitted following (*19*). The protein was concentrated to 40 to 80 mg ml$^{-1}$ using Millipore centricolumns with 50 kDa cutoff. Lipidic Cubic Phase (LCP) for crystallization was obtained in a Hamilton syringe by mixing protein with monoolein (Nu-Chek) in a 42:58 ratio. Subsequently the LCP was slowly injected into another Hamilton syringe filled with crystallization buffer consisting of 100 mM Sorensen buffer pH 5.6 (GERBU) and 30% polyethylene glycol 2000 (Molecular Dimensions). The crystallization was carried out at 21°C and crystals between 15 μm and 50 μm along the longest edge and with a thickness of 1 to 5 μm were obtained within 3 to 6 days (average crystals size 35x35x3 μm). All purification and crystallization steps were performed under dim red light or in the dark.

### Sample preparation for LCP-SFX

The crystallization buffer was removed from LCP containing crystals via a syringe coupler by slow pressing on the syringe plunger. Shortly before the experiment monoolein was added to bring the sample into a homogeneous and transparent LCP mesophase. The sample was supplemented with 5% of MAG 7.9 to prevent phase transition during injection into vacuum and 5% of paraffin was added to support smooth flow of the sample. The crystal density within the sample was homogenized using a custom made "3-way syringe coupler". It consisted of three syringe inlets and the simultaneous passage of sample from two syringes into a third one over several cycles ensured optimal crystal distribution throughout the sample volume for smooth jet operation. The stability of jetting was tested offline with a high-speed camera providing further evidence that the addition of paraffin improved stable jetting. Selected batches of the prepared crystalline sample were tested in advance to confirm high hit rates and diffraction quality using the Swiss Light Source set up for LCP injection (*42*). Before data collection the sample was light adapted at 300 mW for 5 min through a long-pass yellow filter (>515 nm). Sample was used for data collection no longer than 30 min after light exposure to prevent decay of the light adapted dark state. On average, 1 ml of final sample was used per 12-hour shift.

## Data collection

The TR-SFX experiment was performed in June 2017 in the microfocus chamber of the CXI beamline at LCLS (*43*) with the integrated optical pump-probe laser set-up (*44*). The 50 fs XFEL pulses at 9.5 keV were delivered at 120 Hz into a vacuum chamber. In the experiment we used a modified version of the LCP injector (*20*) with a larger sample reservoir of 130 μl to allow a longer data collection and the higher flow rates (2.5 μl min$^{-1}$ through a 50 μm diameter nozzle and, for a small amount of data, 5 μl min$^{-1}$ through a 75 μm diameter nozzle) necessary for time-resolved crystallography (*24*). The LCP stream was aligned with the x-ray beam and an Ti:Sapphire-pump Optical Parametric Amplifier producing optical laser pulses with a 30 Hz repetition rate, 100 fs pulse length, 529 nm wavelength and 17 μJ energy in a focal spot of 95 μm (1/$e^2$). The arrival time of the optical laser pulse relative to the XFEL pulse, was monitored using the timing tool at LCLS (*25, 45*) with nominal time delays Δ$t$ = –500 fs, 300 fs, 600 fs, 900 fs, 1100 fs, and 10 ps. As the exact timing is subject to jitter, data collected at these delays were sorted and binned after collection based on their timing tool signal (see Data sorting and binning). By combining all indexed patterns from the second XFEL pulse after the pump laser excitation (175 μm from the interaction region) we could further resolve Δ$t$ = 8.33 ms, but with lower occupancy due to this time point being excited further from the pump laser peak intensity (fig. S1). We obtained a high quality dark dataset (table S1) by merging patterns of the fourth XFEL pulse after light excitation from all datasets. For clarity, the 120 Hz XFEL, 30 Hz optical data collection scheme is further illustrated in fig. S1.

An important parameter for a successful TR-SFX experiment is the laser power density at sample position, which is critical for efficient activation but difficult to estimate. In our case we aligned the laser approximately 50 μm below the x-ray interaction region to exclude light contamination of the following pulses. This shift reduced the nominal laser power density of 2.4 TW/cm$^2$ to 0.324 TW/cm$^2$ [factor of 0.135 (1/$e^{-2}$)] at the x-ray interaction region. This value is in a similar range as in previously published ultrafast TR-SFX studies (*16, 17, 46*). Using an offline setup with a continuous laser we established that scattering from the 50 μm wide LCP jet (without protein or crystals) reduces the incident laser light by about 80%. Scattering from the LCP jet and the high optical density of the crystals further reduced the average light intensity any given bR molecule was exposed to. Taking the typical crystal dimensions of 35x35x3 μm$^3$ and the parameters above into account, we estimate 3.3 to 0.6 absorbed photons per retinal depending on the orientation of the crystal with respect to the laser pulse. This exposure is within the range where multiphoton effects are negligible in a crystallographic analysis based on the small spectroscopic effect under similar laser conditions (*46–48*). Moreover, our setup provided comparable results to our previous experiment using a nano-

second pump laser with much lower power density (0.06 GW cm$^{-2}$) at SACLA (*19*), with a twisted retinal at 10 ps and 16 ns (fig. S7). The two delays correspond to the lower and upper end of the temporal range where the K intermediate of bR is observed spectroscopically and the high similarity between the two structures indicates that productive photocycles can be induced using a femtosecond laser pump pulse. The similarity of structures for 10 ps/16 ns provides us with an internal control for the presented experiments in the femtosecond range.

Our choice of laser energy was guided by two previous TR-SFX experiments with very similar femtosecond pump laser parameters but different laser energies (fig. S9). In December 2015, we used 8 μJ and 12 μJ, with the former yielding nearly flat Fourier difference electron density maps while the latter provided very weak signal with a few peaks at 3.5 σ and the estimated activation levels of about 5%. In July 2014, we used 20 μJ which yielded about 13% activation levels (*24*). In the currently reported experiment we aimed for activation levels better than 10% and measured all time delays with a consistent 17 μJ in order to collect interpretable crystallographic data.

## Data sorting and binning

Diffraction images were selected with Cheetah (*49*) followed by further sorting according to event codes corresponding to one of the four images collected after the optical laser pulse.

Light data in the femtosecond range were sorted by pump-probe delay time using the timing tool available at CXI with yttrium aluminum garnet (YAG) target (*45*). The spectrally encoded delay was determined by the standard matched-filter procedure implemented in psana, the LCLS-provided analysis software (*50*). Strong etalon effects caused by the thick YAG target necessitated one modification to this standard analysis. Before edge-position determination by matched filtering, the spectral signal was bandstop filtered using a 5th-order Butterworth filter with a cut-on and cut-off frequency of 45 fs$^{-1}$ and 120 fs$^{-1}$ respectively, effectively removing signal oscillations due to etalon. The data where initially sorted into 20 bins with 10,000 images each (see fig. S1). For calculating structural snapshots, we combined 3 overlapping bins which lead to 18 snapshots in the femtosecond range, which we further complement with data collected at Δ$t$ =10 ps and 8.33 ms (see table S1).

## Data processing

The images were indexed using mosflm and dirax indexing algorithms on the peaks identified by Cheetah. Data were integrated (the integration radius was 3 pixels for the peak region and 4 to 7 pixels for the background annulus with integrating 1.2 nm$^{-1}$ beyond the conservative resolution limit determined on a per image basis) and merged with CrystFEL (*51*) version 0.6.3. A geometry refinement using geoptimiser was carried out on a subset of images that diffracted beyond 2.0 Å in CrystFEL's conservative apparent resolution. This step improved high-resolution statistics after reindexing and reintegration of the data.

The indexing ambiguity in space group P6$_3$ was resolved using ambigator in CrystFEL (52). Data were scaled and merged using partialator in CrystFEL without the calculation of partialities (–model = unity), using one cycle of scaling and applying the option to extend the conservative resolution limit determined on the per image basis ("–pushres 1.2"). A small subset of patterns (11,758) with HPLC back pressures 25 bars above the average value for each data run was discarded in order to eliminate any source of potential light contamination in dark data due to occasional jet slowdowns owing to higher crystal density.

### Data analysis

For the structure determination of the dark state, diffraction images from every fourth diffraction image after the optical laser pulse were used. The signal recorded by the timing tool for every first diffraction image after the optical laser pulse was used to sort the diffraction images after the experiment into bins with defined time ranges (see Data processing and binning). Each of the datasets (table S1) consists of three overlapping original bins (fig. S1). The time ranges used for data analysis were initially chosen to contain around 30,000 images (about 27,000 after indexing, see table S1) to ensure good quality data for analysis and to be comparable to the number of images collected at 10 ps. The resolution cutoff for the light data was established so that most datasets have at least a CC* of 0.5 at 1.50 Å. We used a dark dataset of 29,461 patterns collected without optical pump laser to cross-check our high quality dark dataset for light contamination and could not observe difference density peaks corresponding to the M-state above the noise level of 2.5σ.

### Structure determination and refinement of the bR dark state

PDB entry with accession code 5J7A (24) with all water molecules and lipids removed was used as molecular replacement model in Phaser (53). The resting state structure was obtained with several cycles of building and refinement using COOT (54) and PHENIX (55) to a resolution of 1.5 Å (table S2).

### Calculation of difference Fourier density maps

The difference Fourier density maps were calculated with phenix.fobs_minus_fobs_map (55) including the multiscaling feature and low resolution cutoff at 4.5 Å. The electron density peak minima and maxima in σ units (= root mean square electron density of the unit cell) were extracted in COOT (56). Table S3 lists peak values for regions of the density map which at any point in the ultrafast time range exceeded ± 4σ. The values below 2.5σ were set to 0 as being of too low significance.

### Refinement of intermediate states

In a TR-SFX experiment, crystals subjected to optical laser light pulse contain a mixture containing light activated molecules and dark state molecules. We used extrapolated structure factors F$_{ext}$ (57) to enable modeling of bacteriorhodopsin activated states, similar approach as used to model the subpicosecond structural states of PYP (17). The extrapolated structure factors were calculated using a linear approximation (58) as follows: F$_{ext}$ = [(F$_{obs}^{light}$ – F$_{obs}^{dark}$) / activated fraction] + F$_{obs}^{dark}$. The 2F$_{ext}$ – F$_{calc}$ maps calculated with phases of the dark state model showed distinct features in agreement with the F$_{obs}^{light}$ – F$_{obs}^{dark}$ Fourier difference maps. Using this comparison, the light activated fraction of molecules in the data time ranges 49 to 406 fs, 457 to 646 fs, 10 ps, and 8.3 ms was estimated to be 25%, 18%, 16%, and 10% corresponding to fractions where the features associated exclusively with the dark state disappear from extrapolated maps. Reciprocal space refinement against the F$_{ext}$ to 1.9 Å resolution in PHENIX (55) in combination with real space fitting in COOT (56) provided models (table S2) for the respective time points with all of them showing about 98% of residues in the Ramachandran favored region. A comparison of calculated (F$_{calc}^{refined}$ – F$_{calc}^{dark}$) and experimental (F$_{obs}^{light}$ – F$_{obs}^{dark}$) difference densities (fig. S8) was used as additional control to validate the refined structures. Comparison of the bR 8.33 ms structure obtained from the refinement against the extrapolated structure factors with the 1.725 ms structure (19) obtained by an alternative conformation refinement approach shows a high level of similarity between the structures derived using the two different approaches (fig. S6).

### QM/MM calculations

We used a hybrid quantum mechanics/molecular mechanics (QM/MM) method to study the photochemical reaction of bR. The key step in setting up such a QM/MM calculation is the partitioning of the total system in QM and MM subsystems. The QM subsystem is described using a quantum chemical method, while the MM subsystem is computed by a classical force field. Following the crystallographic results, we included the retinal chromophore and the Lys$^{216}$ sidechain, as well as the counter-ion sidechains Arg$^{82}$, Asp$^{85}$, Asp$^{212}$ and the water molecules Wat$^{402}$, Wat$^{404}$, Wat$^{406}$ to the QM part, while the rest of the protein was treated at the MM level. The MM subsystem is treated using an AMBER force field and interacts with the QM subsection through electrostatic embedding. In all the simulations we have performed, the protein backbone was kept fixed in the crystallographic position and only the QM section and all sidechains, which have at least one atom within 5 Å from the retinal Schiff base and Lys$^{216}$ moiety was allowed to be moved freely in the geometry optimization.

To optimize the geometry in the ground state the QM subsystem was described using the pure-GGA BP86 functional with Grimme's corrections for dispersion interactions and the cc-pVDZ basis set. The difference between the ground and excited state density was computed using CAM-B3LYP and the cc-pVTZ basis set.

## REFERENCES AND NOTES

1. B. R. Rost, F. Schneider-Warme, D. Schmitz, P. Hegemann, Optogenetic Tools for Subcellular Applications in Neuroscience. *Neuron* 96, 572–603 (2017). doi: 10.1016/j.neuron.2017.09.047; pmid: 29096074
2. P. Hamm et al., Femtosecond spectroscopy of the photoisomerisation of the protonated Schiff base of all-trans retinal. *Chem. Phys. Lett.* 263, 613–621 (1996). doi: 10.1016/S0009-2614(96)01269-9
3. O. P. Ernst et al., Microbial and animal rhodopsins: Structures, functions, and molecular mechanisms. *Chem. Rev.* 114, 126–163 (2014). doi: 10.1021/cr4003769; pmid: 24364740
4. K. A. Freedman, R. S. Becker, Comparative investigation of the photoisomerization of the protonated and unprotonated n-butylamine Schiff bases of 9-cis-, 11-cis-, 13-cis-, and all-trans-retinals. *J. Am. Chem. Soc.* 108, 1245–1251 (1986). doi: 10.1021/ja00266a020
5. S. Schenkl, F. van Mourik, G. van der Zwan, S. Haacke, M. Chergui, Probing the ultrafast charge translocation of photoexcited retinal in bacteriorhodopsin. *Science* 309, 917–920 (2005). doi: 10.1126/science.1111482; pmid: 16081732
6. T. Kobayashi, T. Saito, H. Ohtani, Real-time spectroscopy of transition states in bacteriorhodopsin during retinal isomerization. *Nature* 414, 531–534 (2001). doi: 10.1038/35107042; pmid: 11734850
7. J. Herbst, K. Heyne, R. Diller, Femtosecond infrared spectroscopy of bacteriorhodopsin chromophore isomerization. *Science* 297, 822–825 (2002). doi: 10.1126/science.1072144; pmid: 12161649
8. G. H. Atkinson, T. L. Brack, D. Blanchard, G. Rumbles, Picosecond time-resolved resonance Raman spectroscopy of the initial trans to cis isomerization in the bacteriorhodopsin photocycle. *Chem. Phys.* 131, 1–15 (1989). doi: 10.1016/0301-0104(89)87077-6
9. P. Altoè, A. Cembran, M. Olivucci, M. Garavelli, Aborted double bicycle-pedal isomerization with hydrogen bond breaking is the primary event of bacteriorhodopsin proton pumping. *Proc. Natl. Acad. Sci. U.S.A.* 107, 20172–20177 (2010). doi: 10.1073/pnas.1007000107; pmid: 21048087
10. C. Wickstrand, R. Dods, A. Royant, R. Neutze, Bacteriorhodopsin: Would the real structural intermediates please stand up? *Biochim. Biophys. Acta* 1850, 536–553 (2015). doi: 10.1016/j.bbagen.2014.05.021; pmid: 24918316
11. K. Edman et al., High-resolution X-ray structure of an early intermediate in the bacteriorhodopsin photocycle. *Nature* 401, 822–826 (1999). doi: 10.1038/44623; pmid: 10548112
12. B. Schobert, J. Cupp-Vickery, V. Hornak, S. Smith, J. Lanyi, Crystallographic structure of the K intermediate of bacteriorhodopsin: Conservation of free energy after photoisomerization of the retinal. *J. Mol. Biol.* 321, 715–726 (2002). doi: 10.1016/S0022-2836(02)00681-2; pmid: 12206785
13. Y. Matsui et al., Specific damage induced by X-ray radiation and structural changes in the primary photoreaction of bacteriorhodopsin. *J. Mol. Biol.* 324, 469–481 (2002). doi: 10.1016/S0022-2836(02)01110-5; pmid: 12445782
14. R. Neutze, K. Moffat, Time-resolved structural studies at synchrotrons and X-ray free electron lasers: Opportunities and challenges. *Curr. Opin. Struct. Biol.* 22, 651–659 (2012). doi: 10.1016/j.sbi.2012.08.006; pmid: 23021004
15. J. Tenboer et al., Time-resolved serial crystallography captures high-resolution intermediates of photoactive yellow protein. *Science* 346, 1242–1246 (2014). doi: 10.1126/science.1259357; pmid: 25477465
16. T. R. M. Barends et al., Direct observation of ultrafast collective motions in CO myoglobin upon ligand dissociation. *Science* 350, 445–450 (2015). doi: 10.1126/science.aac5492; pmid: 26359336
17. K. Pande et al., Femtosecond structural dynamics drives the trans/cis isomerization in photoactive yellow protein. *Science* 352, 725–729 (2016). doi: 10.1126/science.aad5081; pmid: 27151871
18. N. Coquelle et al., Chromophore twisting in the excited state of a photoswitchable fluorescent protein captured by time-resolved serial femtosecond crystallography. *Nat. Chem.* 10, 31–37 (2018). doi: 10.1038/nchem.2853; pmid: 29256511
19. E. Nango et al., A three-dimensional movie of structural changes in bacteriorhodopsin. *Science* 354, 1552–1557 (2016). doi: 10.1126/science.aah3497; pmid: 28008064
20. U. Weierstall et al., Lipidic cubic phase injector facilitates membrane protein serial femtosecond crystallography. *Nat. Commun.* 5, 3309 (2014). doi: 10.1038/ncomms4309; pmid: 24525480

21. E. M. Landau, J. P. Rosenbusch, Lipidic cubic phases: A novel concept for the crystallization of membrane proteins. *Proc. Natl. Acad. Sci. U.S.A.* **93**, 14532–14535 (1996). doi: 10.1073/pnas.93.25.14532; pmid: 8962086

22. S. Boutet, G. J. Williams, The Coherent X-ray Imaging (CXI) instrument at the Linac Coherent Light Source (LCLS). *New J. Phys.* **12**, 035024 (2010). doi: 10.1088/1367-2630/12/3/035024

23. P. Emma et al., First lasing and operation of an ångstrom-wavelength free-electron laser. *Nat. Photonics* **4**, 641–647 (2010). doi: 10.1038/nphoton.2010.176

24. P. Nogly et al., Lipidic cubic phase injector is a viable crystal delivery system for time-resolved serial crystallography. *Nat. Commun.* **7**, 12314 (2016). doi: 10.1038/ncomms12314; pmid: 27545823

25. M. Harmand et al., Achieving few-femtosecond time-sorting at hard X-ray free-electron lasers. *Nat. Photonics* **7**, 215–218 (2013). doi: 10.1038/nphoton.2013.11

26. R. González-Luque et al., Computational evidence in favor of a two-state, two-mode model of the retinal chromophore photoisomerization. *Proc. Natl. Acad. Sci. U.S.A.* **97**, 9379–9384 (2000). doi: 10.1073/pnas.97.17.9379; pmid: 10944211

27. S. Schenkl et al., Insights into excited-state and isomerization dynamics of bacteriorhodopsin from ultrafast transient UV absorption. *Proc. Natl. Acad. Sci. U.S.A.* **103**, 4101–4106 (2006). doi: 10.1073/pnas.0506303103; pmid: 16537491

28. G. H. Atkinson, L. Ujj, Y. Zhou, Vibrational Spectrum of the J-625 Intermediate in the Room Temperature Bacteriorhodopsin Photocycle. *J. Phys. Chem. A* **104**, 4130–4139 (2000). doi: 10.1021/jp9918306

29. A. Warshel, Bicycle-pedal model for the first step in the vision process. *Nature* **260**, 679–683 (1976). doi: 10.1038/260679a0; pmid: 1264239

30. A. Warshel, Z. T. Chu, Nature of the Surface Crossing Process in Bacteriorhodopsin: Computer Simulations of the Quantum Dynamics of the Primary Photochemical Event. *J. Phys. Chem. B* **105**, 9857–9871 (2001). doi: 10.1021/jp010704a

31. M. Sheves, N. Friedman, A. Albeck, M. Ottolenghi, Primary photochemical event in bacteriorhodopsin: Study with artificial pigments. *Biochemistry (Mosc.)* **24**, 1260–1265 (1985). doi: 10.1021/bi00326a031

32. L. Song, M. A. El-Sayed, J. K. Lanyi, Protein catalysis of the retinal subpicosecond photoisomerization in the primary process of bacteriorhodopsin photosynthesis. *Science* **261**, 891–894 (1993). doi: 10.1126/science.261.5123.891; pmid: 17783735

33. T. Yamato, T. Kakitani, Molecular Dynamics Simulation of the Excited-State Dynamics of Bacteriorhodopsin. *Photochem. Photobiol.* **66**, 735–740 (1997). doi: 10.1111/j.1751-1097.1997.tb03217.x

34. F. Gai, K. C. Hasson, J. C. McDonald, P. A. Anfinrud, Chemical dynamics in proteins: The photoisomerization of retinal in bacteriorhodopsin. *Science* **279**, 1886–1891 (1998). doi: 10.1126/science.279.5358.1886; pmid: 9506931

35. M. Shibata, H. Kandori, FTIR studies of internal water molecules in the Schiff base region of bacteriorhodopsin. *Biochemistry* **44**, 7406–7413 (2005). doi: 10.1021/bi050122+; pmid: 15895984

36. S. Shim, J. Dasgupta, R. A. Mathies, Femtosecond time-resolved stimulated Raman reveals the birth of bacteriorhodopsin's J and K intermediates. *J. Am. Chem. Soc.* **131**, 7592–7597 (2009). doi: 10.1021/ja809137x; pmid: 19441850

37. D. Arnlund et al., Visualizing a protein quake with time-resolved X-ray scattering at a free-electron laser. *Nat. Methods* **11**, 923–926 (2014). doi: 10.1038/nmeth.3067; pmid: 25108686

38. L. U. L. Brinkmann, J. S. Hub, Ultrafast anisotropic protein quake propagation after CO photodissociation in myoglobin. *Proc. Natl. Acad. Sci. U.S.A.* **113**, 10565–10570 (2016). doi: 10.1073/pnas.1603539113; pmid: 27601659

39. M. Levantino et al., Ultrafast myoglobin structural dynamics observed with an X-ray free-electron laser. *Nat. Commun.* **6**, 6772 (2015). doi: 10.1038/ncomms7772; pmid: 25832715

40. A. Ansari et al., Protein states and proteinquakes. *Proc. Natl. Acad. Sci. U.S.A.* **82**, 5000–5004 (1985). doi: 10.1073/pnas.82.15.5000; pmid: 3860839

41. P. Nogly et al., Lipidic cubic phase serial millisecond crystallography using synchrotron radiation. *IUCrJ* **2**, 168–176 (2015). doi: 10.1107/S2052252514026487; pmid: 25866654

42. T. Weinert et al., Serial millisecond crystallography for routine room-temperature structure determination at synchrotrons. *Nat. Commun.* **8**, 542 (2017). doi: 10.1038/s41467-017-00630-4; pmid: 28912485

43. M. Liang et al., The Coherent X-ray Imaging instrument at the Linac Coherent Light Source. *J. Synchrotron Radiat.* **22**, 514–519 (2015). doi: 10.1107/S160057751500449X; pmid: 25931062

44. M. P. Minitti et al., Optical laser systems at the Linac Coherent Light Source. *J. Synchrotron Radiat.* **22**, 526–531 (2015). doi: 10.1107/S1600577515006244; pmid: 25931064

45. M. R. Bionta et al., Spectral encoding of x-ray/optical relative delay. *Opt. Express* **19**, 21855–21865 (2011). doi: 10.1364/OE.19.021855; pmid: 22109037

46. B. Schmidt et al., Excited-state dynamics of bacteriorhodopsin probed by broadband femtosecond fluorescence spectroscopy. *Biochim. Biophys. Acta Bioenerg.* **1706**, 165–173 (2005). doi: 10.1016/j.bbabio.2004.10.008; pmid: 15620377

47. A. C. Florean et al., Control of retinal isomerization in bacteriorhodopsin in the high-intensity regime. *Proc. Natl. Acad. Sci. U.S.A.* **106**, 10896–10900 (2009). doi: 10.1073/pnas.0904589106; pmid: 19564608

48. V. I. Prokhorenko et al., Coherent control of retinal isomerization in bacteriorhodopsin. *Science* **313**, 1257–1261 (2006). doi: 10.1126/science.1130747; pmid: 16946063

49. A. Barty et al., *Cheetah*: Software for high-throughput reduction and analysis of serial femtosecond X-ray diffraction data. *J. Appl. Crystallogr.* **47**, 1118–1131 (2014). doi: 10.1107/S1600576714007626; pmid: 24904246

50. D. Damiani et al., Linac Coherent Light Source data analysis using psana. *J. Appl. Crystallogr.* **49**, 672–679 (2016). doi: 10.1107/S1600576716004349

51. T. A. White et al., CrystFEL: A software suite for snapshot serial crystallography. *J. Appl. Crystallogr.* **45**, 335–341 (2012). doi: 10.1107/S0021889812002312

52. W. Brehm, K. Diederichs, Breaking the indexing ambiguity in serial crystallography. *Acta Crystallogr. D Biol. Crystallogr.* **70**, 101–109 (2014). doi: 10.1107/S1399004713025431; pmid: 24419383

53. A. J. McCoy et al., Phaser crystallographic software. *J. Appl. Crystallogr.* **40**, 658–674 (2007). doi: 10.1107/S0021889807021206; pmid: 19461840

54. P. Emsley, K. Cowtan, *Coot*: Model-building tools for molecular graphics. *Acta Crystallogr. D Biol. Crystallogr.* **60**, 2126–2132 (2004). doi: 10.1107/S0907444904019158; pmid: 15572765

55. P. D. Adams et al., *PHENIX*: Building new software for automated crystallographic structure determination. *Acta Crystallogr. D Biol. Crystallogr.* **58**, 1948–1954 (2002). doi: 10.1107/S0907444902016657; pmid: 12393927

56. P. Emsley, B. Lohkamp, W. G. Scott, K. Cowtan, Features and development of Coot. *Acta Crystallogr. D Biol. Crystallogr.* **66**, 486–501 (2010). doi: 10.1107/S0907444910007493; pmid: 20383002

57. M. Schmidt, in *Ultrashort Laser Pulses in Biology and Medicine*, M. Braun, P. Gilch, W. Zinth, Eds. (Springer, 2008), pp. 201–241.

58. U. K. Genick et al., Structure of a protein photocycle intermediate by millisecond time-resolved crystallography. *Science* **275**, 1471–1475 (1997). doi: 10.1126/science.275.5305.1471; pmid: 9045611

59. R. A. Mathies, C. H. Brito Cruz, W. T. Pollard, C. V. Shank, Direct observation of the femtosecond excited-state cis-trans isomerization in bacteriorhodopsin. *Science* **240**, 777–779 (1988). doi: 10.1126/science.3363359; pmid: 3363359

60. E. F. Pettersen et al., UCSF Chimera—a visualization system for exploratory research and analysis. *J. Comput. Chem.* **25**, 1605–1612 (2004). doi: 10.1002/jcc.20084; pmid: 15264254

## ACKNOWLEDGMENTS

### SUPPLEMENTARY MATERIALS

# Science

## Retinal isomerization in bacteriorhodopsin captured by a femtosecond x-ray laser

Przemyslaw Nogly, Tobias Weinert, Daniel James, Sergio Carbajo, Dmitry Ozerov, Antonia Furrer, Dardan Gashi, Veniamin Borin, Petr Skopintsev, Kathrin Jaeger, Karol Nass, Petra Båth, Robert Bosman, Jason Koglin, Matthew Seaberg, Thomas Lane, Demet Kekilli, Steffen Brünle, Tomoyuki Tanaka, Wenting Wu, Christopher Milne, Thomas White, Anton Barty, Uwe Weierstall, Valerie Panneels, Eriko Nango, So Iwata, Mark Hunter, Igor Schapiro, Gebhard Schertler, Richard Neutze and Jörg Standfuss

**Look fast**

Organisms from bacteria to humans sense and react to light. Proteins that contain the light-sensitive molecule retinal couple absorption of light to conformational changes that produce a signal or move ions across a membrane. Nogly *et al.* used an x-ray laser to probe the earliest structural changes to the retinal chromophore within microcrystals of the ion pump bacteriorhodopsin (see the Perspective by Moffat). The excited-state retinal wiggles but is held in place so that only one double bond of retinal is capable of isomerizing. A water molecule adjacent to the proton-pumping Schiff base responds to changes in charge distribution in the chromophore even before the movement of atoms begins.

*Science*, this issue p. eaat0094; see also p. 127

| | |
|---|---|
| **ARTICLE TOOLS** | http://science.sciencemag.org/content/361/6398/eaat0094 |
| **SUPPLEMENTARY MATERIALS** | http://science.sciencemag.org/content/suppl/2018/06/13/science.aat0094.DC1 |
| **RELATED CONTENT** | http://science.sciencemag.org/content/sci/361/6398/127.full |
| **REFERENCES** | This article cites 60 articles, 18 of which you can access for free http://science.sciencemag.org/content/361/6398/eaat0094#BIBL |
| **PERMISSIONS** | http://www.sciencemag.org/help/reprints-and-permissions |

Use of this article is subject to the Terms of Service